Spectral element method for band structures of three-dimensional anisotropic photonic crystals

Ma Luo and Qing Huo Liu
Department of Electrical and Computer Engineering, Duke University, Durham, North Carolina 27708, USA
(Received 1 July 2009; published 9 November 2009)

A spectral element method (SEM) is introduced for accurate calculation of band structures of three-dimensional anisotropic photonic crystals. The method is based on the finite-element framework with curvilinear hexahedral elements. Gauss-Lobatto-Legendre polynomials are used to construct the basis functions. In order to suppress spurious modes, mixed-order vector basis functions are employed and the Bloch periodic boundary condition is imposed into the basis functions with tangential components at the boundary by multiplying a Bloch phase factor. The fields and coordinates in the curvilinear hexahedral elements are mapped to the reference domain by covariant mapping, which preserves the continuity of tangential components of the field. Numerical results show that the SEM has exponential convergence for both square-lattice and triangular-lattice photonic crystals. The sampling density as small as 3.4 points per wavelength can achieve accuracy as high as 99.9%. The band structures of several modified woodpile photonic crystals are calculated by using the SEM.

DOI: 10.1103/PhysRevE.80.056702 PACS number(s): 02.70.Hm, 42.70.Qs, 42.25.Fx, 52.40.Db

I. INTRODUCTION

In order to investigate the physical properties of photonic crystals (PCs) [1–3] and engineer the application of these novel artificial materials, a high accuracy and high efficiency solver for band structures of PCs is necessary. The band structures contain much information about the PCs such as the existence of a band gap, density of states, and propagation properties given by group velocity. Recently, many optical and microwave devices have been constructed using PCs such as high-Q factor optical cavity [4] and light emission controller [5]. Understanding the complete band structures of PCs is very helpful for the design of these devices.

One of the recently most popular methods for the determination of band structures of PCs is the plane-wave expansion (PWE) method [6,7]. The advantage of this method is being free of spurious modes because the basis functions are transverse waves. However, the solutions converge relatively slowly in this method, thus, a very fine grid is required to obtain high accuracy. Another widely used method is the finite element method (FEM) [8,9], which discretizes the system by an unstructured mesh. For the case of full vector wave equation, mixed-order Nedelec basis functions are introduced to suppress the spurious modes [10]. On the other hand, the solutions of FEM also converge slowly. Much more than 10 points per wavelength (PPW) are needed to obtain high accuracy with error smaller than 0.1%.

Recently, the pseudospectral time-domain and pseudospectral frequency-domain methods [11–14] have been introduced to the calculation of electromagnetic fields with high accuracy. A multidomain pseudospectral method solver was developed to solve band structures of two-dimensional PCs [15]. This method shows a fast exponential convergence.

On the other hand, a spectral element method (SEM) [16–20] is developed for high accuracy and high efficiency simulation of various fields. We have used SEM to calculate the band structures of two-dimensional PCs consisting of isotropic, anisotropic, and dispersive materials [21,22]. SEM is a special kind of high-order FEM, which uses Gauss-Lobatto-Legendre (GLL) polynomials to construct the basis functions. In our implementation, analytic mapping between the reference domain and real space is used to increase the accuracy. The solutions converge exponentially at a very high speed. The exponential convergence speed remains the same even for triangular-lattice PCs and anisotropic material PCs. In this paper, the SEM is extended to solve band structures of three-dimensional (3D) photonic crystals. In order to suppress the spurious modes, mixed-order vector basis functions based on GLL polynomials are used.

The paper is organized as follows. In Sec. II, the process of discretization of the system into a matrix equation given by SEM is explained. In Sec. III, numerical results of band structures of PCs are shown. Several cases are investigated including square-lattice PCs with only orthogonal elements and with nonorthogonal elements, triangular-lattice PCs, and some more complicated structures based on woodpile PCs. Finally, Sec. IV gives a brief conclusion.

II. FORMULATION

A. 3D Helmholtz equations and SEM functionals for anisotropic PCs

For a frequency domain 3D electromagnetic problem in a medium with arbitrary anisotropy, the electric and magnetic fields can be described by full vector Helmholtz equations

$$\nabla \times [\mu_r^{-1}(\nabla \times \mathbf{E})] - k_0^2 \varepsilon_r \mathbf{E} = \mathbf{0}, \tag{1}$$

$$\nabla \times [\varepsilon_r^{-1}(\nabla \times \mathbf{H})] - k_0^2 \mu_r \mathbf{H} = \mathbf{0}, \tag{2}$$

where $k_0 = \omega/c$ is the wave number in vacuum; ε_r and μ_r are the 3×3 relative permittivity and relative permeability tensors. Since the equations for electric field and magnetic field are dual to each other, below we will only discuss the formulas for the electric field, and the formulas for the magnetic field are the same except for exchanging the position of permittivity and permeability.

In a unit cell of the PC, the fields satisfy the Bloch periodic boundary condition. For both electric field $\mathbf{E}$ and magnetic field $\mathbf{H}$, the tangential components are continuous at an interface between different dielectric materials. As a result, the boundary conditions can be written as

$$\mathbf{E}_{\parallel}(\mathbf{r}+\mathbf{R}) = \mathbf{E}_{\parallel} e^{-j\mathbf{k}\cdot\mathbf{R}}. \tag{3}$$

Here $\mathbf{E}_{\parallel}$ is the tangential component of electric field at the boundary of the unit cell, $\mathbf{r}$ is the position vector at the boundary, and $\mathbf{R}$ can be written as

$$\mathbf{R} = l\mathbf{a}_1 + m\mathbf{a}_2 + n\mathbf{a}_3, \tag{4}$$

where $(\mathbf{a}_1, \mathbf{a}_2, \mathbf{a}_3)$ are the three primitive lattice vectors of the unit cell, (l,m,n) are three integers that make $(\mathbf{r}+\mathbf{R})$ become a position vector of the boundary at the opposite face, and $\mathbf{k}$ is the Bloch wave vector.

In order to formulate the functional for a variational method, Eq. (1) is integrated through the whole unit cell after being dot multiplied by its complex conjugate field $\mathbf{E}^*$ from the left side. After integration by parts and the use of the Bloch periodic boundary condition, the functional can be written as

$$F(\mathbf{E}) = \int_{\Omega} d\mathbf{r}\{(\nabla \times \mathbf{E}^*) \cdot \mu_r^{-1} (\nabla \times \mathbf{E}) - k_0^2 \mathbf{E}^* \cdot \varepsilon_r \mathbf{E}\}, \tag{5}$$

where Ω is the integration region of the unit cell. The boundary integrations on opposite faces have opposite signs, thus, making the total boundary integration term vanish. The discretization process of SEM is based on this functional in Eq. (5).

B. Mixed-order GLL basis functions and discretization

In order to discretize the problem, the unit cell is meshed by nonoverlapping curvilinear hexahedral elements conforming to the geometry. The coordinates and field in each element are mapped to the reference domain and the field is expanded by mixed-order vector basis functions. The reference domain is defined as $(\xi,\eta,\zeta) \in [-1,1]$. The mixed-order vector basis functions are constructed by the GLL polynomials [16,18],

$$\phi_j^{(N)}(\xi) = \frac{-1}{N(N+1)L_N(\xi_j^{(N)})} \frac{(1-\xi^2)L_N'(\xi)}{(\xi - \xi_j^{(N)})}, \tag{6}$$

where N is the order of the GLL polynomial, $L_N(\xi)$ is the Nth-order Legendre polynomial and $L_N'(\xi)$ is its derivative, and $\xi_j^{(N)}$ is the $(j+1)$th zero point of $(1-\xi^2)L_N'(\xi)=0$ within $\xi \in [-1,1]$ with $j=0,1,\ldots,N$. $\xi_j^{(N)}$ is called the nodal point of the Nth-order GLL polynomial. Given all the $N+1$ nodal points, the Nth-order GLL polynomials in Eq. (6) can be easily written as

$$\phi_j^{(N)}(\xi) = \prod_{i \neq j} \frac{(\xi - \xi_i^{(N)})}{(\xi_j^{(N)} - \xi_i^{(N)})}, \quad j = 0,1,\ldots,N. \tag{7}$$

The mixed-order vector GLL basis functions in the reference domain are given by

$$\tilde{\mathbf{\Phi}}_{rst}^{\xi} = \hat{\xi} \phi_r^{(N-1)}(\xi) \phi_s^{(N)}(\eta) \phi_t^{(N)}(\zeta), \tag{8}$$

$$\tilde{\mathbf{\Phi}}_{rst}^{\eta} = \hat{\eta} \phi_r^{(N)}(\xi) \phi_s^{(N-1)}(\eta) \phi_t^{(N)}(\zeta), \tag{9}$$

$$\tilde{\mathbf{\Phi}}_{rst}^{\zeta} = \hat{\zeta} \phi_r^{(N)}(\xi) \phi_s^{(N)}(\eta) \phi_t^{(N-1)}(\zeta). \tag{10}$$

The point $(\xi_r^{(N-1)}, \eta_s^{(N)}, \zeta_t^{(N)})$ is called the nodal point of the mixed-order vector basis function at the ξ direction because at this point the ξ component of the basis function equals 1. The same property applies to nodal points of the other two directions. Making covariant mapping from the reference domain to the real space gives the mixed-order vector GLL basis functions in the real space, $\mathbf{\Phi}_{rst}^{\xi}(x,y,z)$, $\mathbf{\Phi}_{rst}^{\eta}(x,y,z)$, and $\mathbf{\Phi}_{rst}^{\zeta}(x,y,z)$. The covariant mapping ensures that the tangential components at the surface of the elements are continuous as detailed in the next subsection.

The electric field in one element is interpolated by the mixed-order vector basis functions and the field value at the corresponding nodal points. Since the tangential components of electric field at any interface are continuous, the mapping between the indices of basis functions of the global system and the indices of the elemental GLL basis functions at each element obeys the following rule: if the global basis function is associated with a nodal point interior to an element, it is the same as the elemental GLL basis function with the same nodal point; if the global basis function is associated with a normal direction nodal point at the surface of an element, it is also the same as the elemental GLL basis function with the same nodal point; if the global basis function is associated with a tangential direction nodal point at the surface of an element, it has support on all the other elemental GLL basis functions having nodal points in the same direction and located at the same position of the surface of adjacent elements. Defining a compound index for the basis function of the global system, $j=\{\hat{u},r,s,t\}$, where $\hat{u}=(\hat{\xi},\hat{\eta},\hat{\zeta})$, the electric field in the real space can be expanded as

$$\mathbf{E} = \sum_j E_j \mathbf{\Phi}_j. \tag{11}$$

Inserting Eq. (11) into functional (5), and applying the variational principle, the Helmholtz equation is discretized into a generalized eigenvalue matrix equation

$$\mathbf{SE} = k_0^2 \mathbf{ME}, \tag{12}$$

where $\mathbf{E}$ is now the column vector of electric field at all of the nodal points $E_1, E_2, \ldots$, and $\mathbf{S}$ and $\mathbf{M}$ are the stiffness matrix and mass matrix. The stiffness matrix and mass matrix are the assembling of elemental stiffness and mass matrices from the N_e elements in one unit cell of the PC,

$$\mathbf{S} = \sum_{e=1}^{N_e} \mathbf{S}^{(e)}, \quad \mathbf{M} = \sum_{e=1}^{N_e} \mathbf{M}^{(e)}. \tag{13}$$

The elemental stiffness and mass matrices of the eth element $\mathbf{S}^{(e)}$ and $\mathbf{M}^{(e)}$ are

$$S_{j,k}^{(e)} = \int_{\Omega_e} d\mathbf{r} (\nabla \times \mathbf{\Phi}_j) \cdot \mu_r^{-1} \cdot (\nabla \times \mathbf{\Phi}_k), \tag{14}$$

$$M_{j,k}^{(e)} = \int_{\Omega_e} d\mathbf{r}\boldsymbol{\Phi}_j \cdot \varepsilon_r \cdot \boldsymbol{\Phi}_k, \tag{15}$$

where the integration region Ω_e covers the space in the eth element. Rather than imposing the Bloch periodic boundary condition on the field, here we impose this periodic condition with the Bloch phase in the basis functions with nodal points located at the unit cell boundary. For example, for the left boundary nodal point $\mathbf{r}$ with tangential direction and the corresponding right boundary point $\mathbf{r}+\mathbf{a}_1$, they have the same basis function (thus, one unknown field coefficient), but with a Bloch phase $e^{-j\mathbf{k}\cdot\mathbf{R}}$ ($\mathbf{R}=\mathbf{a}_1$ here) multiplied to the GLL basis function at the right boundary point. By solving eigenvalue problem (12) with different Bloch wave vectors, the band structure of the 3D PC is obtained.

C. Covariant mapping between a curved element and the reference domain

Since the GLL basis functions are defined in the reference domain, it is more convenient to calculate the integration of Eqs. (14) and (15) in the reference domain. In order to keep the tangential components continuous, covariant mapping is used. Given the mapping of coordinates from the real space to the reference domain,

$$x = x(\xi,\eta,\zeta), \quad y = y(\xi,\eta,\zeta), \quad z = z(\xi,\eta,\zeta), \tag{16}$$

the Jacobian matrix is defined as

$$\mathbf{J} = \begin{bmatrix} \frac{\partial x}{\partial \xi} & \frac{\partial y}{\partial \xi} & \frac{\partial z}{\partial \xi} \\ \frac{\partial x}{\partial \eta} & \frac{\partial y}{\partial \eta} & \frac{\partial z}{\partial \eta} \\ \frac{\partial x}{\partial \zeta} & \frac{\partial y}{\partial \zeta} & \frac{\partial z}{\partial \zeta} \end{bmatrix} \tag{17}$$

and the covariant mapping between fields in a curved element in the real space and in the reference domain is given by [23]

$$\boldsymbol{\Phi}_{r,s,t}^{u}(x,y,z) = \mathbf{J}^{-1}\tilde{\boldsymbol{\Phi}}_{r,s,t}^{u}(\xi,\eta,\zeta),$$

$$\nabla \times \boldsymbol{\Phi}_{r,s,t}^{u}(x,y,z) = \frac{1}{\det(\mathbf{J})}\mathbf{J}^{T}\tilde{\nabla} \times \tilde{\boldsymbol{\Phi}}_{r,s,t}^{u}(\xi,\eta,\zeta). \tag{18}$$

If the nodal point of an elemental basis function in the reference domain is located at the surface, it only has either normal component or tangential component of this surface. The normal component basis function has only normal component after covariant mapping; but the tangential component basis functions in general have both tangential and normal components after covariant mapping. The tangential components depend only on the shape of the surface, so the elemental basis function of the adjacent elements of the same surface with nodal point located at the same place and with the same direction has the same tangential component. Since these two elemental basis functions are supported by the same basis function, this basis function keeps the tangential component continuous; and because the elemental basis function with a normal component does not have a tangential component after covariant mapping, it does not break the continuity of tangential components. As a result, this set of basis functions under the definition of covariant mapping preserves the continuity of tangential components at any interface. After being mapped into the reference domain, the elemental matrices of matrix elements in Eqs. (14) and (15) become

$$S_{j,k}^{(e)} = \int_{-1}^{1}\int_{-1}^{1}\int_{-1}^{1} d\xi d\eta d\zeta \det(\mathbf{J})(\mathbf{f}_j)^* \cdot \mu_r^{-1} \cdot (\mathbf{f}_k), \tag{19}$$

$$M_{j,k}^{(e)} = \int_{-1}^{1}\int_{-1}^{1}\int_{-1}^{1} d\xi d\eta d\zeta \det(\mathbf{J})(\mathbf{J}^{-1}\tilde{\boldsymbol{\Phi}}_j)^* \varepsilon_r (\mathbf{J}^{-1}\tilde{\boldsymbol{\Phi}}_k), \tag{20}$$

where $\tilde{\boldsymbol{\Phi}}_j$ and $\mathbf{f}_j$ are complex due to the Bloch periodic condition, and

$$\mathbf{f}_j \equiv \frac{1}{\det(\mathbf{J})}\mathbf{J}^{T}\tilde{\nabla} \times \tilde{\boldsymbol{\Phi}}_j(\xi,\eta,\zeta). \tag{21}$$

The GLL quadrature integration method is used to calculate the integral in the reference domain.

D. Diagonal mass matrix and regular eigenvalue problem

The Nth-order GLL quadrature integration method is exact for integration of $(2N-1)$th order polynomials. When the element is orthogonal, the Jacobian matrix is a constant matrix, so that the integrals in Eqs. (19) and (20) contain only GLL polynomials. Since mixed-order vector basis functions are used, the polynomials being integrated in the mass matrix are either $2N$th order or $(2N-2)$th order. If $(N+1)$th (or Nth) order GLL quadrature integration is used for the $2N$th [or $(2N-2)$th] order polynomial, the elemental mass matrix is exact but is not diagonal. In contrast, if Nth [or $(N-1)$th] order GLL quadrature integration is used for the $2N$th [or $(2N-2)$th] order polynomials, the elemental mass matrix is not exact but is diagonal. If all elements are orthogonal, the global mass matrix is diagonal with this approximate integration. Then, the general eigenvalue problem (12) can be reduced to a regular eigenvalue problem

$$\tilde{\mathbf{S}}\tilde{\mathbf{E}} = k_0^2\tilde{\mathbf{E}}, \tag{22}$$

where

$$\tilde{\mathbf{E}} = \mathbf{M}^{1/2}\mathbf{E}, \quad \tilde{\mathbf{S}} = \mathbf{M}^{-1/2}\mathbf{S}\mathbf{M}^{-1/2}. \tag{23}$$

The new stiffness matrix $\tilde{\mathbf{S}}$ has the same sparseness as $\mathbf{S}$. Numerical results of this GLL approximation SEM show that the results converge to the SEM results with exact integration. However, this approximation cannot be used for magneto-optical materials, which have imaginary nondiagonal permittivity (or permeability).

III. NUMERICAL EXAMPLES

Below we show numerical results of (a) square-lattice PCs with only orthogonal elements and with curved ele-

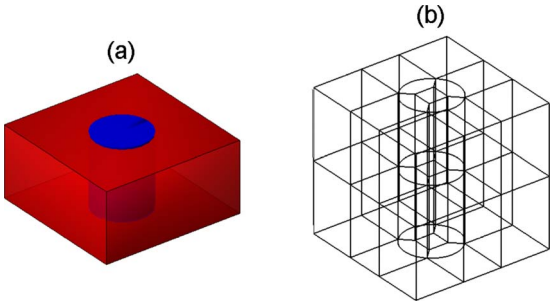

FIG. 1. (Color online) (a) The dielectric structure of the lower half of one unit cell of a layered square-lattice air-hole slab PC with outer (inner) region being dielectric material (air). (b) The SEM mesh of the unit cell conforming to the dielectric structure.

ments, (b) triangular-lattice PCs, and (c) woodpile PCs with an air hole or yttrium iron garnet (YIG) cylinder at the junction. Convergence behaviors are tested and efficiency of the SEM is compared with the PWE method.

A. Square-lattice PCs

The first example is a 3D PC consisting of infinite layers of square-lattice air-hole slabs. The unit cell is an $a \times a \times a$ cube, with upper half being air, lower half being a slab with an air hole in the middle as shown in Fig. 1(a), and a being the period of the square-lattice PC. The relative permittivity of the slabs is 12. The radius of the hole is $0.3a$. The SEM mesh conforming to the dielectric structure in one unit cell is shown in Fig. 1(b). The band structure calculated by the fourth-order SEM is plotted as solid lines in Fig. 2(a) together with that calculated by the PWE in software MPB [6]. It is confirmed that the SEM gives a correct band structure. Note that there are discrepancies for higher bands between the SEM and the PWE, but the characteristics of these band structures are the same, especially the degeneracy at the high symmetry point of the first Brillouin zone. As a result, these

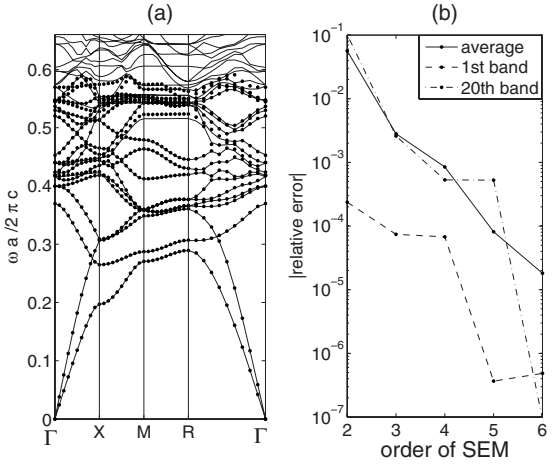

FIG. 2. SEM results for the layered square-lattice air-hole PC in Fig. 1. (a) Band structure calculated by the fourth-order SEM (solid line) and PWE (dots). (b) Average relative error of the lowest 20 modes, relative error of the first band and the 20th band, respectively, at the M point of the band structure versus the SEM order.

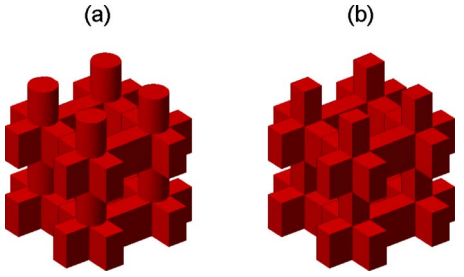

FIG. 3. (Color online) The dielectric structure of $2 \times 2 \times 2$ unit cells of a square-lattice PC with (a) a circular cylinder and (b) a rectangular cylinder in the middle of the upper level. The permittivity of the circular and rectangular cylinder rods is 12.

discrepancies are caused by accuracy differences. Figure 2(b) shows the average relative error of the lowest 20 modes at the M point versus the order of SEM, as well as the relative error of the first and the 20th bands. Since the highest-order numerical result we have calculated is the seventh-order SEM, the relative error is calculated by comparing the SEM results with the seventh-order SEM result. The lower band has smaller error than the higher band as expected. The curves of the relative error of the individual band look like a stair function that the results of adjacent two orders of SEM have almost the same error and the results of the next two higher orders of SEM have a much smaller error. This is because the mixed-order basis functions contain both Nth- and $(N-1)$th-order GLL polynomials. Thus, the SEM with two orders higher can improve the accuracy of interpolation significantly. The curve of the average relative error of the lowest 20 bands is smooth, although each curve of error of individual band looks like a stair function. As a result, we only discuss the average error in the rest of the paper, and the results of individual bands have similar accuracy. It is shown that the solutions converge exponentially as the order increases. Because the average vacuum wavelength of the lowest 20 modes is about $2a$, and the vector basis functions are in mixed order, the smallest sampling density of the Nth-order SEM mesh is about $1.2 \times (N-1)$ PPW, which is calculated along the height of the slabs. From Fig. 2(b), the fourth-order SEM has a relative error smaller than 0.1%, which means that the SEM with a sampling density as small as 3.4 PPW can have accuracy high enough for engineering applications.

Another more complicated structure modeled is a square-lattice PC shown in Fig. 3(a), which is the dielectric structure of $2 \times 2 \times 2$ unit cells. The radius and height of the rods are $0.2a$ and $0.5a$, respectively; the height of rectangular cylinders is also $0.5a$ and their width is $0.2\sqrt{2}a$. The band structure of this PC is shown in Fig. 4. Note that there is not a complete band gap, but the lowest two bands are completely separated from the other higher bands. Numerical simulation shows that the PC of the same structure with a larger permittivity value has a complete band gap above the lowest two bands. The average relative error of the lowest 20 modes at the R point of the structure given by the SEM versus its order is plotted in Fig. 5(a). As a comparison, the average relative error from the PWE method implemented by MPB versus the grid resolution is plotted in Fig. 5(b). The relative error from

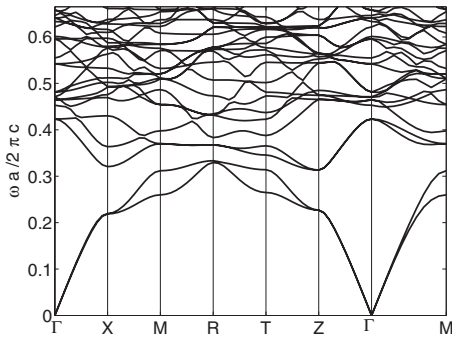

FIG. 4. Band structure of the square-lattice PC in Fig. 3(a).

the PWE method is calculated by comparing its result with that in a grid resolution of 80. The SEM mesh of this system is the same as that of the previous examples, but the distribution of dielectric material of this system is more complicated. The convergence behaviors for this system become somewhat worse for the higher-order SEM because there are more interfaces with discontinuous distribution of materials. When there is an interface separating two different materials, the normal component electric field is not continuous and the interpolation at this interface generates more errors. The GLL polynomials used in the higher-order SEM can improve the accuracy of the interpolation of continuous functions within each element, but cannot improve the interpolation at the interface. Since there are more interfaces with discontinuous distribution of material in this system, they generate more errors, and thus the convergence behaviors become worse. However, the fourth-order SEM still has an error less than 0.1%. Comparison of CPU time and number of unknowns for this accuracy between the SEM and PWE is shown in Table I, as detailed below. For the same accuracy, the PWE needs at least 72 grid resolution requiring at least $72\times72\times72=373\,248$ unknowns. Calculation of the lowest 20 eigenmodes at one k point by using MPB with a grid resolution of 72 needs 1200 s, so it needs 84 000 s to calculate the whole band structure with 70 k points. On the other hand, the fourth-order SEM has only 4992 unknowns. It needs 484 s to calculate stiffness and mass matrix elements, and 60 s to calculate the lowest 20 eigenmodes for each k point, so in total it needs 4684 s to calculate the whole band

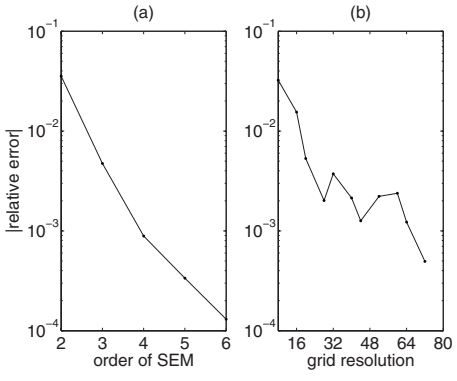

FIG. 5. Average relative error of the lowest 20 modes at the R point of the band structure in Fig. 4 calculated by (a) SEM versus its order and (b) PWE versus its grid resolution.

TABLE I. CPU time for calculating the band structure of the square-lattice PC in Fig. 3(a) with 20 bands and 70 k points, and the number of unknowns of the fourth-order SEM and PWE implemented by MPB with a grid resolution of 72.

	CPU time (s)	Number of unknowns
SEM	4684	4992
PWE	373248	84000

structure, which is 18 times faster than the PWE.

If the circular cylinder rods in Fig. 3(a) are changed to rectangular rods with the same width, $0.2\sqrt{2}a$, as shown in Fig. 3(b), all elements of SEM mesh are orthogonal. Thus, the GLL approximation can be used to reduce the generalized eigenvalue problem into a regular eigenvalue problem. The band structure of this system is shown in Fig. 6(a) and the relative error versus the order of SEM is shown in Fig. 6(b). It is observed that the SEM with GLL approximation integral has exponential convergence, with a slightly slower speed than the SEM with exact integration. For the fifth-order SEM, the GLL approximation result has an error less than 0.1% and the solution converges to the exact integration result.

B. Triangular-lattice PCs

A PC consisting of infinite layers of triangular-lattice air-hole slabs is also calculated by the fourth-order SEM. The circular air hole is centered and has a diameter of $0.3a$ with a being the distance between the neighboring holes. The band structure is shown in Fig. 7(a) (solid line) together with the band structure calculated by PWE (dots), and the relative error is plotted in Fig. 7(b). As the figures show, the numerical result of SEM is confirmed by numerical result of PWE implemented by MPB. The discrepancies between the two methods for higher bands are due to different accuracies. The solutions of the SEM converge exponentially with the same speed for triangular-lattice and for square-lattice PCs. The fourth-order SEM has a relative error as small as 0.1%, and

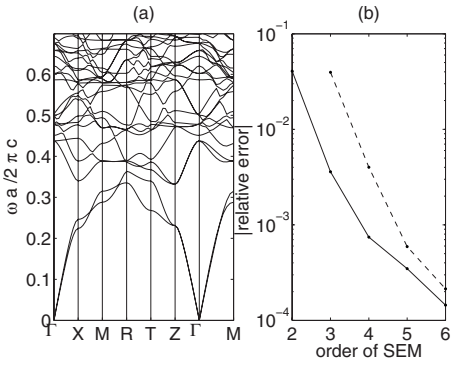

FIG. 6. (a) Band structure of the square-lattice PC in Fig. 3(b). (b) Relative error of SEM with exact integration (solid line) and with GLL approximate integration (dashed line) versus the order of SEM.

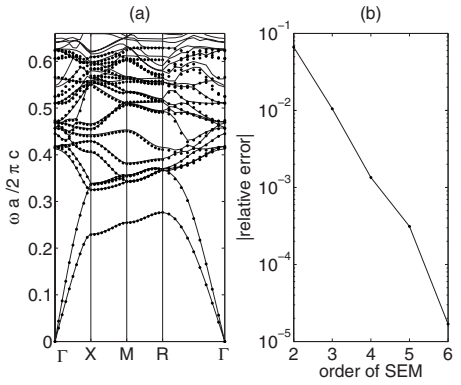

FIG. 7. SEM results for a layered triangular-lattice air-hole slab PC with diameter $0.3a$ with a being distance between neighboring holes. (a) Band structure calculated by the fourth-order SEM (solid line) and PWE (dots). (b) Average relative error of the lowest 20 modes at the M point of the band structure calculated by the SEM versus its order.

the smallest sampling density in the system is 3.4 PPW, along the height of the slabs. As a result, the SEM can also be very efficient for simulation of triangular-lattice PCs.

C. Band structures of woodpile PCs with different modifications

The SEM is used to calculate the band structure of a more complicated woodpile PC shown in Fig. 8 [24,25] inlaid with circular cylinder rods at each junction. The dimensions of the woodpile PC are as follows: the height of the wood is 200 nm, the width is 180 nm, and the period in one layer is 650 nm. This woodpile PC is widely investigated for its large complete band gap and for its potential usage in high-Q resonators or other nanophotonic devices. The radius of the rods is 60 nm. The rods can be air holes or can be filled with other materials. Figure 9(a) is the band structure of the PC without

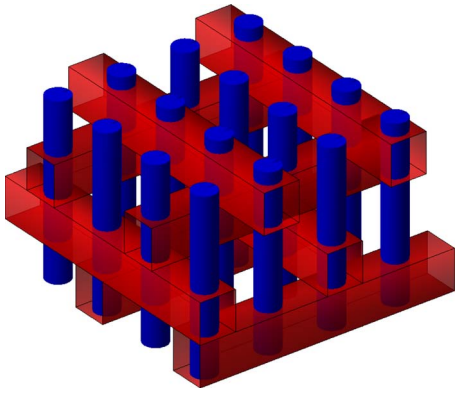

FIG. 8. (Color online) The dielectric structure of $2\times2\times1$ unit cells of a woodpile PC (rectangular blocks, red online) inlaid with circular cylinder rods (circular cylinders, blue online) at each junction. The rods can be air hole or YIG. For the woodpile structure, the height of the wood is 200 nm, the width is 180 nm, and the period in one layer is 650 nm. The radius of the rods is 60 nm and the centers of the rods are located at the centers of the junctions.

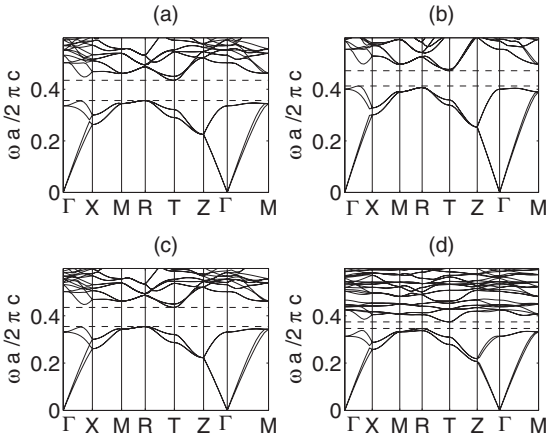

FIG. 9. (a) Band structure of woodpile PC shown in Fig. 8 without the circular cylinder rods. (b) Band structure of the same woodpile PC with the air rods. (c) and (d) are band structures of the same woodpile PC with the rods being YIG without and with magnetic field of 1600 G applied parallel to the rods. $a=650$ nm is the period in each layer.

the rods as comparison. Our numerical result is confirmed by comparing the band gap to the theoretical result from Ref. [25]. Figure 9(b) is the band structure of the PC inlaid with the air rods. It is shown that the width of the band gap is smaller and the center of the band gap becomes higher. Figures 9(c) and 9(d) are the band structures of the PC inlaid with YIG rods, which is a multiferroic material. The permittivity of YIG is 15. If there is no applied magnetic field, the permeability is 1. In this case, the band structure is plotted in Fig. 9(c). When a static external magnetic field of 1600 G is applied parallel to the rods, the permeability of YIG becomes anisotropic [26] and is given as

$$\mu_r = \begin{bmatrix} 14 & -j12.4 & 0 \\ j12.4 & 14 & 0 \\ 0 & 0 & 1 \end{bmatrix}. \quad (24)$$

In this case, the band structure is shown in Fig. 9(d). It can be found that the width of the band gap becomes smaller and the center of the band gap becomes lower. These numerical results show that the band gap of the woodpile PCs inlaid with cylinder rods can be modified by changing the material of the rods or by changing the external magnetic field. These properties could be useful for the design of tunable nanophotonic devices.

IV. CONCLUSION

The full vector spectral element method, a higher-order finite element method, has been developed to solve band structures of 3D photonic crystals. GLL polynomials are used to construct the mixed-order vector basis functions to suppress the spurious modes with nonzero eigenvalues. The convergence is shown to be exponential for both square-lattice and triangular-lattice PCs. In order to obtain acceptable accuracy, i.e., a relative error as small as 0.1%, only 3.4 PPW is needed. When all meshing elements are orthogonal,

the GLL approximation integration can be used to yield a diagonal mass matrix, thus, reducing the generalized eigenvalue problem to a regular eigenvalue problem. Numerical results show that under this approximation, the SEM solutions still converge exponentially. The SEM is applied to calculate band structures of several PCs with complicated dielectric structures including the woodpile PCs inlaid with circular cylinder rods at the junctions. The band structures show tunability of the band gap by changing the material filled in the rods or by changing the external magnetic field.

ACKNOWLEDGMENT

The support from the National Science Foundation under Grant No. CCF-0621862 is appreciated.

[1] E. Yablonovitch, Phys. Rev. Lett. **58**, 2059 (1987).
[2] S. John, Phys. Rev. Lett. **58**, 2486 (1987).
[3] J. D. Joannopoulos, *Photonic Crystals: Molding the Flow of Light*, 2nd ed. (Princeton University Press, Princeton, 2008).
[4] Y. Akahane, T. Asano, B.-S. Song, and S. Noda, Nature (London) **425**, 944 (2003).
[5] S. Ogawa, M. Imada, S. Yoshimoto, M. Okano, and S. Noda, Science **305**, 227 (2004).
[6] S. G. Johnson and J. D. Joannopoulos, Opt. Express **8**, 173 (2001).
[7] K. M. Ho, C. T. Chan, and C. M. Soukoulis, Phys. Rev. Lett. **65**, 3152 (1990).
[8] B. G. Ward, IEEE J. Quantum Electron. **44**, 150 (2008).
[9] P. Sotirelis and J. D. Albrecht, Phys. Rev. B **76**, 075123 (2007).
[10] J. S. Savage and A. F. Peterson, IEEE Trans. Microwave Theory Tech. **44**, 874 (1996).
[11] Q. H. Liu, Microwave Opt. Technol. Lett. **15**, 158 (1997).
[12] B. Yang, D. Gottlieb, and J. S. Hesthaven, J. Comput. Phys. **134**, 216 (1997).
[13] G.-X. Fan, Q. H. Liu, and J. S. Hesthaven, IEEE Trans. Geosci. Remote Sens. **40**, 1366 (2002).
[14] Q. H. Liu, IEEE Antennas Wireless Propag. Lett. **1**, 131 (2002).
[15] P.-J. Chiang, C.-P. Yu, and H.-C. Chang, Phys. Rev. E **75**, 026703 (2007).
[16] G. C. Cohen, *Higher-Order Numerical Methods for Transient Wave Equations* (Springer, New York, 2001).
[17] J.-H. Lee and Q. H. Liu, IEEE Trans. Comput.-Aided Des. **24**, 1848 (2005).
[18] J.-H. Lee, T. Xiao, and Q. H. Liu, IEEE Trans. Microwave Theory Tech. **54**, 437 (2006).
[19] J.-H. Lee and Q. H. Liu, IEEE Trans. Microwave Theory Tech. **55**, 983 (2007).
[20] A. T. Patera, J. Comput. Phys. **54**, 468 (1984).
[21] M. Luo, Q. H. Liu, and Z. Li, Phys. Rev. E **79**, 026705 (2009).
[22] M. Luo and Q. H. Liu, J. Opt. Soc. Am. A Opt. Image Sci. Vis. **26**, 1598 (2009).
[23] A. F. Peterson, S. L. Ray, and R. Mittra, *Computational Methods for Electromagnetics* (IEEE Press, Piscataway, NJ, 1997).
[24] S. Noda, K. Tomoda, N. Yamamoto, and A. Chutinan, Science **289**, 604 (2000).
[25] B. Gralak, M. de Dood, G. Tayeb, S. Enoch, and D. Maystre, Phys. Rev. E **67**, 066601 (2003).
[26] Z. Wang, Y. D. Chong, J. D. Joannopoulos, and M. Soljacic, Phys. Rev. Lett. **100**, 013905 (2008).